

Research



Cite this article: Protonotarios NE, Fokas AS, Kostarellos K, Kastis GA. 2018 The attenuated spline reconstruction technique for single photon emission computed tomography.

J. R. Soc. Interface **15**: 20180509.

<http://dx.doi.org/10.1098/rsif.2018.0509>

Received: 6 July 2018

Accepted: 31 October 2018

Subject Category:

Life Sciences – Mathematics interface

Subject Areas:

medical physics

Keywords:

single photon emission computed tomography (SPECT), analytic image reconstruction, attenuated Radon transform

Author for correspondence:

Nicholas E. Protonotarios

e-mail: protost@hotmail.com

Electronic supplementary material is available online at <https://dx.doi.org/10.6084/m9.figshare.c.4302725>.

The attenuated spline reconstruction technique for single photon emission computed tomography

Nicholas E. Protonotarios^{1,2}, Athanassios S. Fokas^{1,3,6}, Kostas Kostarellos^{4,5} and George A. Kastis¹

¹Research Center of Mathematics, Academy of Athens, Athens 11527, Greece

²Department of Mathematics, National Technical University of Athens, Zografou Campus, Athens 15780, Greece

³Department of Applied Mathematics and Theoretical Physics, University of Cambridge, Cambridge CB3 0WA, UK

⁴Nanomedicine Laboratory, Faculty of Biology, Medicine and Health, University of Manchester, Manchester M13 9PL, UK

⁵National Graphene Institute, University of Manchester, Manchester M13 9PL, UK

⁶Department of Electrical Engineering, University of Southern California, Los Angeles, CA 90089, USA

NEP, 0000-0002-7701-5644; KK, 0000-0002-2224-6672; GAK, 0000-0002-1283-0883

We present the *attenuated spline reconstruction technique* (aSRT) which provides an innovative algorithm for single photon emission computed tomography (SPECT) image reconstruction. aSRT is based on an analytic formula of the inverse attenuated Radon transform. It involves the computation of the Hilbert transforms of the linear attenuation function and of two sinusoidal functions of the so-called *attenuated sinogram*. These computations are achieved by employing the attenuation information provided by computed tomography (CT) scans and by utilizing custom-made cubic spline interpolation. The purpose of this work is: (i) to present the mathematics of aSRT, (ii) to reconstruct simulated and real SPECT/CT data using aSRT and (iii) to evaluate aSRT by comparing it to filtered backprojection (FBP) and to ordered subsets expectation minimization (OSEM) reconstruction algorithms. Simulation studies were performed by using an image quality phantom and an appropriate attenuation map. Reconstructed images were generated for 45, 90 and 180 views over 360 degrees with 20 realizations and involved Poisson noise of three different levels (NL), namely 100% (NL1), 50% (NL2) and 10% (NL3) of the total counts, respectively. Moreover, real attenuated SPECT sinograms were reconstructed from a real study of a Jaszczak phantom, as well as from a real clinical myocardial SPECT/CT study. Comparisons between aSRT, FBP and OSEM reconstructions were performed using contrast, bias and image roughness. The results suggest that aSRT can efficiently produce accurate attenuation-corrected reconstructions for simulated and real phantoms, as well as for clinical data. In particular, in the case of the clinical myocardial study, aSRT produced reconstructions with higher cold contrast than both FBP and OSEM. aSRT, by incorporating the attenuation correction within itself, may provide an improved alternative to FBP. This is particularly promising for ‘cold’ regions as those occurring in myocardial ischaemia.

1. Introduction

Single photon emission computed tomography (SPECT) is an important nuclear medicine modality with vast preclinical and clinical applications, especially in the medical fields of cardiology and neurology. This emission tomography technique provides information regarding functional aspects of a patient’s organs, particularly the heart and the brain (functional cardiac and functional brain imaging).

SPECT utilizes the unique chemical characteristics of decaying radiopharmaceuticals, consisting of a targeting agent labelled with a radioisotope, such as technetium (⁹⁹Tc). The radiopharmaceutical is introduced into the patient intravenously and it is distributed in the body in a fashion governed by its

biochemical properties [1]. The injected radiotracers radiate single photons and the detectors count these individual photons (γ -ray events) [2].

Nuclear medicine image reconstruction is performed, as in all tomography-related inverse problems, by reconstructing projection data, usually stored in the form of sinograms [3]. There exist several reconstruction algorithms, characterized either as analytic or iterative. The prevailing analytic image reconstruction technique is *filtered backprojection* (FBP), whereas the predominant iterative image reconstruction approach is *ordered subsets expectation maximization* (OSEM). In this work, we shall focus on analytic reconstruction techniques, assuming parallel-beam geometry.

Attenuation correction is an important part of the SPECT reconstruction process, especially in the context of myocardial perfusion imaging [4]. It is often even considered as the potential ‘holy grail’ of the SPECT imaging field [5]. The main objective of attenuation correction is to minimize false-positive defects, so that attenuation-corrected reconstructions would allow for better quantification of abnormalities [6]. However, until quite recently (early 2000s), only less than 10% of SPECT cameras worldwide were equipped with attenuation correction systems [7]. Nowadays, hybrid SPECT/CT is becoming a standard dual medical imaging modality, with various SPECT/CT systems being currently commercially available. This dual imaging modality is now suitable for a vast variety of diagnostic applications with clinical impact, essentially addressing the ultimate goal in nuclear medicine of shortening the acquisition time and of providing accurate, attenuation-corrected fusion imaging [8].

SPECT reconstruction algorithms aim to invert the so-called *attenuated Radon transform*, which constitutes a certain generalization of the two-dimensional Radon transform. The attenuated Radon transform is the line integral of the distribution of the radioactive material inside the patient’s body, attenuated with respect to the associated linear attenuation coefficient. SPECT data are usually stored as camera projections, which can be expressed as attenuated sinograms, similar to the sinograms of positron emission tomography (PET). The analytical approach to SPECT reconstruction involves the *inverse attenuated Radon transform* (IART), i.e. the inversion of the attenuated sinogram. An explicit mathematical formulation of IART is given in [9], following the pioneering work of Novikov [10]. Other analytical SPECT reconstruction techniques based on Novikov’s work [10] include Natterer’s inversion formulæ [11], Kunyansky’s elegant reconstruction algorithm [12] (also viewed as a generalization of the seminal Tretaiik–Metz algorithm [13] which is further improved by Metz & Pan [14]), and Bal and Moireau’s method [15]. Furthermore, Ammari *et al.* [16] provide a closely related asymptotic imaging technique in photoacoustics, in the presence of wave attenuation. The numerical implementation of all these analytic algorithms is based on the concept of filtered backprojection: these numerical techniques employ the convolution property of the Fourier transform in order to compute the Hilbert transform involved in IART and apply appropriate filters for the cancellation of high frequencies.

In this paper, we present an alternative numerical technique for the numerical evaluation of the IART occurring in SPECT, namely the *attenuated spline reconstruction technique* (aSRT) for SPECT. aSRT is a novel two-dimensional analytic image reconstruction algorithm, which is based on a new, improved

mathematical derivation of an earlier implementation presented in [9]. Instead of the traditional Fourier-based methods, we employ custom-made cubic splines for the computation of the Hilbert transforms of the linear attenuation function and of two sinusoidal functions of the so-called *attenuated sinogram*. We note that the techniques used in [9] and in the present work both employ custom-made cubic splines. Indeed, in our case, we applied splines to compute the Hilbert transform of $\hat{\mu}$ (defined in equation (2.5)), the two sinusoidal functions of the attenuated sinogram, namely G^C and G^S (defined in equations (2.8)) and the function G (defined in equation (2.7)). The corresponding analysis is found in §2.2. These functions are different from the functions encountered in [9] (this becomes clear by comparing equation (3.6) of [9] with equation (2.6) of proposition 2.1 of the present paper). Hence, this new derivation improves substantially the earlier formulation, leading to simplified expressions which have the important advantage that they can be implemented numerically in an efficient way. aSRT, in comparison to FBP and OSEM, has the advantage of incorporating attenuation correction within itself. Furthermore, all necessary calculations are performed in the physical (image) space, as opposed to the Fourier space.

It is important to note how aSRT differs from SRT for PET [17,18]. aSRT constitutes a substantial generalization over SRT: SRT aims to invert the non-attenuated Radon transform, i.e. the line integrals of the radioactive distribution, while aSRT inverts the corresponding line integrals attenuated with respect to the linear attenuation function (μ). Although in both PET and SPECT the transmitted gamma rays suffer a relative intensity loss, outlined by the well-known Beer’s law, from a mathematical point of view, the inversion occurring in PET is a special case of the corresponding inversion in SPECT. In PET, the attenuation factor is the integral of μ along a single line, whereas in SPECT the attenuation factor is the integral of μ along a single line segment.

The aim of this work is (a) to present the mathematical setting of aSRT, (b) to reconstruct simulated as well as real SPECT/CT data using aSRT in order to evaluate its performance and (c) to compare aSRT with FBP and OSEM. This is the first work involving the analytic inversion of the attenuated Radon transform, where reconstructions of real clinical data are presented, and improved contrast and bias with respect to FBP are demonstrated.

2. Mathematical formulation

2.1. Inverse attenuated Radon transform

Consider a directed line L on the plane specified by two real numbers, namely the signed distance from the origin ρ , $-\infty < \rho < \infty$, and the angle with the x_1 -axis θ , $0 \leq \theta < 2\pi$ (figure 1). The unit vectors parallel (\mathbf{e}^{\parallel}) and perpendicular (\mathbf{e}^{\perp}) to this line are given by

$$\begin{aligned}\mathbf{e}^{\parallel} &= (\cos \theta, \sin \theta), \\ \mathbf{e}^{\perp} &= (-\sin \theta, \cos \theta).\end{aligned}$$

Every point on L in Cartesian coordinates $\mathbf{x} = (x_1, x_2)$ can be expressed in terms of the *local* coordinates (ρ, τ) via the equation

$$\mathbf{x} = \rho \mathbf{e}^{\perp} + \tau \mathbf{e}^{\parallel},$$

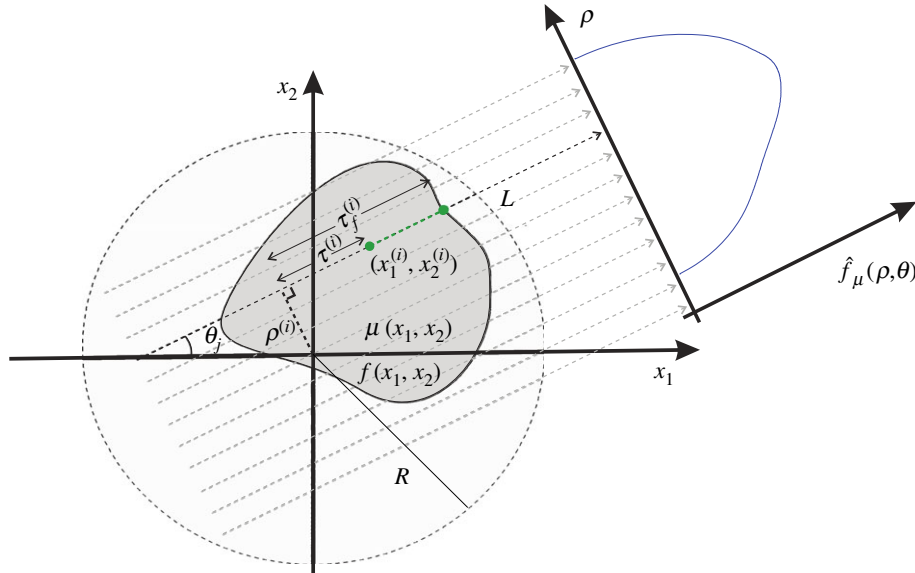


Figure 1. A two-dimensional object, with attenuation coefficient $\mu(x_1, x_2)$, being imaged with parallel-beam projection geometry. Both Cartesian (x_1, x_2) and local (ρ, τ) coordinates are indicated.

where τ is a parameter along L . Hence,

$$x_1 = \tau \cos \theta - \rho \sin \theta \quad (2.1a)$$

and

$$x_2 = \tau \sin \theta + \rho \cos \theta. \quad (2.1b)$$

We can invert equations (2.1) and express the local coordinates (ρ, τ) in terms of the Cartesian coordinates (x_1, x_2) and the associated angle θ :

$$\rho = x_2 \cos \theta - x_1 \sin \theta \quad (2.2a)$$

and

$$\tau = x_2 \sin \theta + x_1 \cos \theta. \quad (2.2b)$$

The line integral of a function $f: \mathbb{R}^2 \rightarrow \mathbb{R}$ attenuated with respect to the attenuation function $\mu: \mathbb{R}^2 \rightarrow \mathbb{R}$ is called the *attenuated Radon transform* of $f(x_1, x_2)$. It is usually stored in the form of the so-called *attenuated sinogram*, denoted by $\hat{f}_\mu(\rho, \theta)$:

$$\begin{aligned} \hat{f}_\mu(\rho, \theta) &= \int_{-\infty}^{\infty} e^{-\int_{\tau}^{\infty} \mu(s \cos \theta - \rho \sin \theta, s \sin \theta + \rho \cos \theta) ds} \\ &\quad \times f(\tau \cos \theta - \rho \sin \theta, \tau \sin \theta + \rho \cos \theta) d\tau, \\ &0 \leq \theta < 2\pi, \quad -\infty < \rho < \infty. \end{aligned} \quad (2.3)$$

Associated with equation (2.3) there exists the following *inverse problem*: given the functions $\mu(x_1, x_2)$, $-\infty < x_1, x_2 < \infty$, and $\hat{f}_\mu(\rho, \theta)$, $0 \leq \theta < 2\pi$, $-\infty < \rho < \infty$, determine the function $f(x_1, x_2)$. The relevant inversion formula, called the IART, was first derived by Novikov [10], extending the derivation of the analogous result for the inverse Radon transform presented in [19]. It was later shown in [9] that the IART formula can actually be obtained via a slight modification of a certain formula contained in [19]. The IART is given by

$$f(x_1, x_2) = \frac{1}{4\pi} (\partial_{x_1} - i\partial_{x_2}) \int_0^{2\pi} e^{i\theta} J(x_1, x_2, \theta) d\theta, \quad -\infty < x_1, x_2 < \infty, \quad (2.4a)$$

where the function J is defined by

$$J(x_1, x_2, \theta) = e^{M(\tau, \rho, \theta)} L_\mu(\rho, \theta) \hat{f}_\mu(\rho, \theta) \Big|_{\substack{\tau=x_2 \sin \theta + x_1 \cos \theta \\ \rho=x_2 \cos \theta - x_1 \sin \theta}} \quad (2.4b)$$

with M and L_μ defined by

$$M(\tau, \rho, \theta) = \int_{\tau}^{\infty} \mu(s \cos \theta - \rho \sin \theta, s \sin \theta + \rho \cos \theta) ds \quad (2.4c)$$

and

$$L_\mu(\rho, \theta) = e^{P^- \hat{\mu}(\rho, \theta)} P^- e^{P^- \hat{\mu}(\rho, \theta)} + e^{-P^+ \hat{\mu}(\rho, \theta)} P^+ e^{P^+ \hat{\mu}(\rho, \theta)}. \quad (2.4d)$$

In equation (2.4d), $\hat{\mu}$ represents the Radon transform of the attenuation function μ , i.e.

$$\begin{aligned} \hat{\mu}(\rho, \theta) &= \int_{-\infty}^{\infty} \mu(\tau \cos \theta - \rho \sin \theta, \tau \sin \theta + \rho \cos \theta) d\tau, \\ &0 \leq \theta < 2\pi, \quad -\infty < \rho < \infty, \end{aligned} \quad (2.4e)$$

with the operators P^\pm denoting the usual projection operators in the variable ρ , i.e.

$$(P^\pm g)(\rho) = \pm \frac{g(\rho)}{2} + \frac{1}{2i\pi} \oint_{-\infty}^{\infty} \frac{g(r)}{r - \rho} dr, \quad -\infty < \rho < \infty, \quad (2.4f)$$

where \oint denotes the principal value integral.

In what follows, it is useful to define F as half the Hilbert transform of $\hat{\mu}$, i.e.

$$F(\rho, \theta) \equiv \frac{1}{2} \mathcal{H} \{ \hat{\mu}(\rho, \theta) \} = \frac{1}{2\pi} \oint_{-\infty}^{\infty} \frac{\hat{\mu}(r, \theta)}{r - \rho} dr, \quad (2.5)$$

where \mathcal{H} denotes the Hilbert transform in the variable ρ .

Proposition 2.1. *The IART formula defined in equation (2.4a) is equivalent to the representation*

$$\begin{aligned} f(x_1, x_2) &= -\frac{1}{2\pi} \int_0^{2\pi} e^{M(\tau, \rho, \theta)} [M_\rho(\tau, \rho, \theta) G(\rho, \theta) \\ &\quad + G_\rho(\rho, \theta)] \Big|_{\substack{\rho=x_2 \cos \theta - x_1 \sin \theta \\ \tau=x_2 \sin \theta + x_1 \cos \theta}} d\theta, \end{aligned} \quad (2.6)$$

where M is defined in equation (2.4c), the subscripts denote differentiation with respect to ρ , and G is defined by

$$G(\rho, \theta) = e^{-(1/2)\hat{\mu}(\rho, \theta)} [\cos(F(\rho, \theta))G^C(\rho, \theta) + \sin(F(\rho, \theta))G^S(\rho, \theta)], \quad (2.7)$$

with the functions G^C and G^S defined by

$$G^C(\rho, \theta) = \frac{1}{2\pi} \oint_{-\infty}^{\infty} e^{(1/2)\hat{\mu}(r, \theta)} \cos F(r, \theta) \frac{\hat{f}_{\mu}(r, \theta) dr}{r - \rho} \quad (2.8a)$$

and

$$G^S(\rho, \theta) = \frac{1}{2\pi} \oint_{-\infty}^{\infty} e^{(1/2)\hat{\mu}(r, \theta)} \sin F(r, \theta) \frac{\hat{f}_{\mu}(r, \theta) dr}{r - \rho}. \quad (2.8b)$$

Proof. We apply the operator L_{μ} which is defined in equation (2.4d), on the attenuated Radon transform \hat{f}_{μ} which is defined in equation (2.3):

$$(L_{\mu} \hat{f}_{\mu})(\rho, \theta) = \{e^{P^- \hat{\mu}(\rho, \theta)} P^- e^{P^- \hat{\mu}(\rho, \theta)} + e^{-P^+ \hat{\mu}(\rho, \theta)} P^+ e^{P^+ \hat{\mu}(\rho, \theta)}\} \hat{f}_{\mu}(\rho, \theta). \quad (2.9)$$

Equations (2.4f) and (2.5) imply

$$e^{P^{\pm} \hat{\mu}} = e^{\pm \hat{\mu}/2 - iF}. \quad (2.10)$$

Hence,

$$e^{P^- \hat{\mu}} P^- \{e^{-P^- \hat{\mu}} \hat{f}_{\mu}\} = e^{-\hat{\mu}/2 - iF} \left[-\frac{1}{2} e^{\hat{\mu}/2 + iF} \hat{f}_{\mu} + \frac{1}{2i} \mathcal{H} \{e^{\hat{\mu}/2 + iF} \hat{f}_{\mu}\} \right] \quad (2.11a)$$

and

$$e^{-P^+ \hat{\mu}} P^+ \{e^{P^+ \hat{\mu}} \hat{f}_{\mu}\} = e^{-\hat{\mu}/2 + iF} \left[\frac{1}{2} e^{\hat{\mu}/2 - iF} \hat{f}_{\mu} + \frac{1}{2i} \mathcal{H} \{e^{\hat{\mu}/2 - iF} \hat{f}_{\mu}\} \right]. \quad (2.11b)$$

Using equations (2.11), as well as the fact that $e^{iF} = \cos F + i \sin F$, we can simplify equation (2.9) as follows (for details, see appendix A):

$$(L_{\mu} \hat{f}_{\mu})(\rho, \theta) = -2iG(\rho, \theta), \quad (2.12)$$

where $G(\rho, \theta)$ is defined in (2.7). It is important to note that equation (2.12) implies that the function $i(L_{\mu} \hat{f}_{\mu})$ is real. Thus, equations (2.4b) and (2.12) imply that

$$J(x_1, x_2, \theta) = -2i[e^{M(\tau, \rho, \theta)} G(\rho, \theta)]_{\substack{\tau=x_2 \sin \theta + x_1 \cos \theta \\ \rho=x_2 \cos \theta - x_1 \sin \theta}}. \quad (2.13)$$

Hence, using the identity

$$(\partial_{x_1} - i\partial_{x_2}) = e^{-i\theta}(\partial_{\tau} - i\partial_{\rho}), \quad (2.14)$$

which arises from the application of the chain rule to the local coordinates defined in equations (2.1), we can calculate the action of the above operator on J :

$$\begin{aligned} (\partial_{x_1} - i\partial_{x_2})J &= -2ie^{-i\theta}(\partial_{\tau} - i\partial_{\rho})[e^{M(\tau, \rho, \theta)} G(\rho, \theta)]_{\substack{\tau=x_2 \cos \theta - x_1 \sin \theta \\ \rho=x_2 \sin \theta + x_1 \cos \theta}} \\ &= -2ie^{-i\theta}[e^M(M_{\tau} - iM_{\rho})G + e^M(G_{\tau} - iG_{\rho})]_{\substack{\rho=x_2 \cos \theta - x_1 \sin \theta \\ \tau=x_2 \sin \theta + x_1 \cos \theta}} \\ &= -2e^{-i\theta}e^M[-i\mu G + M_{\rho}G + G_{\rho}]_{\substack{\rho=x_2 \cos \theta - x_1 \sin \theta \\ \tau=x_2 \sin \theta + x_1 \cos \theta}} \end{aligned} \quad (2.15)$$

where we have used the identities

$$M_{\tau}(\tau, \rho, \theta)|_{\substack{\rho=x_2 \cos \theta - x_1 \sin \theta \\ \tau=x_2 \sin \theta + x_1 \cos \theta}} = \mu(x_1, x_2) \quad \text{and} \quad G_{\rho}(\rho, \theta) = 0.$$

By inserting the operator $(\partial_{x_1} - i\partial_{x_2})$ inside the integral in the right-hand side of equation (2.4a), and by combining equations (2.16) and (2.15), we find

$$f(x_1, x_2) = -\frac{1}{2\pi} \int_0^{2\pi} e^M [-i\mu G + M_{\rho}G + G_{\rho}]_{\substack{\rho=x_2 \cos \theta - x_1 \sin \theta \\ \tau=x_2 \sin \theta + x_1 \cos \theta}} d\theta. \quad (2.16)$$

The first term of the integral on the right-hand side of equation (2.16) can be simplified as follows:

$$\begin{aligned} -i \int_0^{2\pi} \mu(x_1, x_2) [e^{M(\tau, \rho, \theta)} G(\rho, \theta)]_{\substack{\tau=x_2 \sin \theta + x_1 \cos \theta \\ \rho=x_2 \cos \theta - x_1 \sin \theta}} d\theta \\ = \frac{1}{2} \mu(x_1, x_2) \int_0^{2\pi} J(x_1, x_2, \theta) d\theta. \end{aligned} \quad (2.17)$$

Equation (2.9) of [9], with μ replaced by u , evaluated at $\lambda = 0$ yields

$$u(x_1, x_2, 0) = \frac{1}{2\pi} \int_0^{2\pi} J(x_1, x_2, \theta) d\theta.$$

Furthermore, the limit $\lambda \rightarrow 0$ of equation (2.2) of [9] yields

$$\frac{\partial u(x_1, x_2, 0)}{\partial \bar{z}} = 0,$$

which means that u is analytic everywhere, including infinity. Recalling that u satisfies the boundary condition

$$u = O\left(\frac{1}{z}\right), \quad z \rightarrow \infty,$$

it follows that the entire function u vanishes (Liouville's theorem), thus

$$\int_0^{2\pi} J(x_1, x_2, \theta) d\theta = 0. \quad (2.18)$$

Hence, taking into account equation (2.18), equation (2.17) implies that

$$\int_0^{2\pi} \mu(x_1, x_2) [e^{M(\tau, \rho, \theta)} G(\rho, \theta)]_{\substack{\tau=x_2 \sin \theta + x_1 \cos \theta \\ \rho=x_2 \cos \theta - x_1 \sin \theta}} d\theta = 0,$$

and therefore equation (2.4a) becomes equation (2.6). ■

2.2. Numerical implementation of inverse attenuated Radon transform using splines

In order to evaluate all the quantities appearing in equation (2.6), we employ the Gauss–Legendre quadrature for the computation of the function $M(\tau, \rho, \theta)$, as well as piecewise polynomial functions (splines) [20] for the computation of the functions $F(\rho, \theta)$ and $G(\rho, \theta)$. For all the functions involved in IART, we suppose that the evaluation of the solution to the inverse problem (2.4) is performed at the points $\{x_1^{(i)}, x_2^{(j)}\}_{i,j=1}^n$, i.e. in a given square reconstruction grid.

2.2.1. The evaluation of $M(\tau, \rho, \theta)$ and $M_{\rho}(\tau, \rho, \theta)$

The integral (2.4c) involves the computation of the integral of the given attenuation function $\mu(x_1, x_2)$ from $s = \tau^{(i)}$ to $s = \tau_f^{(j)}$; see figure 1. However,

$$(\rho^{(j)})^2 + (\tau_f^{(j)})^2 \leq R^2,$$

where R denotes the radius of the circular path centred at the origin, which encapsulates the support of both functions

$f(x_1, x_2)$ and $\mu(x_1, x_2)$. Hence,

$$M(\tau^{(i)}, \rho^{(i)}, \theta_j) = \int_{\tau^{(i)}}^{\sqrt{R^2 - (\rho^{(i)})^2}} \mu(s \cos \theta_j - \rho^{(i)} \sin \theta_j, s \sin \theta_j + \rho^{(i)} \cos \theta_j) ds. \quad (2.19)$$

This integral can be computed using the Gauss–Legendre quadrature with two functional evaluations at every step, i.e.

$$\int_{\alpha}^{\beta} f(s) ds \sim \frac{1}{2}(\beta - \alpha)[f(\tau_1) + f(\tau_2)],$$

where

$$\tau_1 = \alpha + \left(\frac{1}{2} - \frac{\sqrt{3}}{6}\right)(\beta - \alpha), \quad \tau_2 = \alpha + \left(\frac{1}{2} + \frac{\sqrt{3}}{6}\right)(\beta - \alpha).$$

For the evaluation of $M_\rho(\tau, \rho, \theta)$, we employ an appropriate finite difference scheme, as in [21].

2.2.2. The evaluation of $F(\rho, \theta)$

For the evaluation of $F(\rho, \theta)$, we proceed in a similar way as in [17], but here instead of evaluating the derivative of the Hilbert transform of $\hat{\mu}(\rho, \theta)$, we evaluate the Hilbert transform of $\hat{\mu}(\rho, \theta)$, itself. For details, see appendix B.

2.2.3. The evaluation of $G(\rho, \theta)$ and $G_\rho(\rho, \theta)$

Let f^c and f^s denote the following functions:

$$f^c(\rho, \theta) = e^{(1/2)\hat{\mu}(\rho, \theta)} \cos(F(\rho, \theta)) \hat{f}_\mu(\rho, \theta), \quad 0 \leq \theta < 2\pi, \quad -1 \leq \rho \leq 1, \quad (2.20a)$$

and

$$f^s(\rho, \theta) = e^{(1/2)\hat{\mu}(\rho, \theta)} \sin(F(\rho, \theta)) \hat{f}_\mu(\rho, \theta), \quad 0 \leq \theta \leq 2\pi, \quad -1 \leq \rho \leq 1, \quad (2.20b)$$

where $\hat{\mu}$, \hat{f}_μ and F are defined in equations (2.4e), (2.3) and (2.5), respectively.

We suppose that the attenuated sinogram, $\hat{f}_\mu(\rho, \theta)$, is given at the points $\{\rho_i\}_1^n$. Then, by computing $\hat{\mu}(\rho, \theta)$ and $F(\rho, \theta)$ at these points, we can compute the functions $f^c(\rho, \theta)$ and $f^s(\rho, \theta)$ at the same points. Hence, using equation (2.20), see appendix B, and replacing $f(\rho, \theta)$ by $f^c(\rho, \theta)$ and $f^s(\rho, \theta)$, we can compute $G^c(\rho, \theta)$ and $G^s(\rho, \theta)$, respectively. In order to eliminate the logarithmic singularities of $G^c(\rho, \theta)$ and $G^s(\rho, \theta)$ we require that both f^c and f^s vanish at the endpoints:

$$f^c(-1, \theta) = f^c(1, \theta) = 0 \quad (2.21a)$$

and

$$f^s(-1, \theta) = f^s(1, \theta) = 0. \quad (2.21b)$$

These equations are valid provided that

$$\hat{f}_\mu(-1, \theta) = \hat{f}_\mu(1, \theta) = 0, \quad (2.22)$$

which in nuclear medicine cases is true, due to the fact that we assume that the attenuated sinogram has finite support. By combining $G^c(\rho, \theta)$ and $G^s(\rho, \theta)$, we are able to calculate $G(\rho, \theta)$ as in equation (2.7).

For the numerical evaluation of the derivative of G with respect to ρ , $G_\rho(\rho, \theta)$, we employ a suitable finite difference scheme.

3. Material and methods

3.1. Simulations

3.1.1. Simulated phantom

For the purposes of our simulations, we have modelled a rotating, single-head gamma camera comprising 129 scintillation crystals. The corresponding square image grid size used was 129×129 pixels. The image and detector pixel size was in all simulation studies 4 mm. We have performed an assessment of aSRT by employing simulated data of an image quality (IQ) phantom. This specific phantom has been employed in order to quantitate the ability of each of the above three reconstruction techniques to detect both hot and cold lesions of variable size inside a radioactive background. The IQ phantom consists of four circular hot regions (with diameters of 12.7, 15.9, 19.1 and 25.4 mm, denoted with S_1 to S_4 , respectively) and two circular cold regions (with diameters of 31.8 and 38 mm, denoted with S_5 and S_6 , respectively), inside a larger warm region that simulates the background. The diameter of the larger background circle is 21.6 cm. The radioactive concentration ratio between hot regions and the warm background (α_h/α_b) is 4 : 1 for the four hot regions.

Simulated attenuated sinograms of the IQ phantom were generated in STIR (Software for Tomographic Image Reconstruction) [22] using appropriate attenuation maps. The sinograms were acquired for 45, 90 and 180 views over 360 degrees. Three different noise levels (NL) were investigated: 100% (NL1), 50% (NL2) and 10% (NL3) of the total counts. Using the initial noiseless sinogram (NL0) as the starting point, we generated 20 Poisson-noise realizations at the three different levels (NL1, NL2 and NL3). For 180 views, the noiseless sinograms contain 6×10^6 events, while the noisy sinograms from each noise level contain 6, 3 and 0.6×10^6 events, respectively. Similarly, in the cases of 90 and 45 views, the corresponding numbers of events were 3 (NL0), 3 (NL1), 1.5 (NL2) and 0.3×10^6 (NL3) events, and 1.5 (NL0), 1.5 (NL1), 0.75 (NL2) and 0.15×10^6 (NL3) events, respectively.

3.1.2. Implementation of aSRT, of FBP and of OSEM

aSRT reconstructions

All aSRT reconstructions were performed in Matlab. There was no post-reconstruction filtering applied in these aSRT reconstructions.

FBP reconstructions

All simulated non-corrected FBP reconstructions were generated in the open-source software library STIR [22]. Subsequently, a ramp filter was applied to these reconstructions with a cut-off frequency equal to the Nyquist frequency. It is worth noting that the STIR library does not provide a dedicated routine for attenuation correction for FBP in SPECT/CT. Therefore, all FBP reconstructions were attenuation corrected in Matlab according to the first-order Chang's attenuation correction method. For this purpose, CT attenuation maps were employed as in [23]. We note that Chang's method is by design only an approximate attenuation correction method.

OSEM reconstructions

OSEM attenuation-corrected reconstructions were generated with 5 subsets and 10, 20, 30 and 50 iteration updates, namely OSEM10, OSEM20, OSEM30 and OSEM50, respectively. All OSEM reconstructions were generated in STIR with attenuation correction taken into account; neither scatter correction nor detector/collimator response was modelled.

3.2. Real data

For the purposes of real data reconstructions, we have employed data from a real Jaszczak phantom study as well as from a clinical cardiac study.

3.2.1. Real Jaszczak phantom

We have performed reconstructions of a real Jaszczak phantom, with data provided by a Mediso AnyScan[®] SC SPECT/CT scanner equipped with the Nucline[™] all modality acquisition software. For this technetium (^{99m}Tc) SPECT study, low energy high resolution parallel collimators were used. The attenuated sinograms were provided by Mediso Medical Imaging Systems, Budapest. The phantom is the standard Jaszczak phantom[™] and consists of six cold solid spheres with diameters of 12.7, 15.9, 19.1, 25.4, 31.8 and 38 mm, denoted by S_1 to S_6 , respectively. The number of views used was 128 and the corresponding reconstruction grid size was 256×256 pixels. The image and detector pixel size was 2.13 mm. The number of events per slice was approximately 1.2×10^6 . The total amount of radioactivity in the phantom was 8 mCi (296 MBq) of technetium-99m isotope. The total scan duration was 64 min, corresponding to 30 s acquisition for each of the 128 projections collected. Three realizations ($R = 3$) were utilized during this real phantom SPECT/CT study. We note that the standard Jaszczak phantom involves only cold regions.

3.2.2. Clinical data

Real clinical data were acquired from a GE Millennium VG Hawkeye[™] SPECT/CT system. The Millennium VG camera includes two extra-large rectangular Digital XP detectors, which can image isotopes of energies within the range of 59 keV to 511 keV. A patient was injected with 3 mCi (111 MBq) of the thallium-201 isotope. A sinogram of this myocardial perfusion ²⁰¹Tl stress study was acquired for 60 views and was reconstructed using aSRT, FBP and OSEM in a 64×64 reconstruction grid. All necessary corrections (attenuation, scatter, detector/collimator response, etc.) were performed according to the manufacturer's suggested clinical protocol. The image and detector pixel size was 7.81 mm. The number of events per slice was approximately 1.4×10^6 . The total scan duration was 17 min, corresponding to 17 s acquisition for each of the 60 projections collected.

3.3. Image metrics

In order to determine the quality of the reconstructed images of the phantoms investigated, a region of interest (ROI) analysis was performed. Comparisons with FBP and OSEM were performed evaluating contrast, bias and image roughness, as described below and in [18,24]. The following image quality metrics were calculated: (a) hot region contrast, C_h , (b) cold region contrast, C_c , (c) %bias for hot regions, b_h , (d) bias % of background for cold regions, b_c and (e) background image roughness, IR . In order to determine the ROI statistics at each solid sphere, circular ROIs were employed in Matlab. The diameters of all ROIs were the same as the diameters of the lesions being measured. Several image metrics were calculated for all noise levels and averaged over all realizations, R .

The hot region contrast (C_h) was calculated for each hot circular region using the following equation [17]:

$$C_h = \frac{1}{R} \sum_{r=1}^R \frac{m_{h,r}/m_{b,r} - 1}{a_h/a_b - 1}, \quad (3.1)$$

where $m_{h,r}$ and $m_{b,r}$ are the average counts (mean pixel value) measured in each hot sphere and in the background ROI, respectively, for each realization, r , and a_h and a_b are the actual radioactivity of each hot region and the background, respectively. In the case of the simulated IQ phantom used, the ratio (a_h/a_b) is four. We note that C_h is also referred to in the literature as contrast recovery coefficient.

In a similar manner, the cold region contrast (C_c) was calculated for each cold circular region using the equation

$$C_c = 1 - \frac{1}{R} \sum_{r=1}^R \frac{m_{c,r}}{m_{b,r}}, \quad (3.2)$$

where $m_{c,r}$ are the average counts (mean pixel value) measured in each cold circular region and in the background ROI.

The %bias for hot spheres (b_h) for each hot circular region was calculated using the equation

$$b_h = \frac{100}{a_h} \times \left[\frac{1}{R} \sum_{r=1}^R (m_{h,r} - a_h) \right], \quad (3.3)$$

and the bias % of background for cold regions (b_c) for each cold circular region was calculated via the formula

$$b_c = \frac{100}{a_b} \times \left(\frac{1}{R} \sum_{r=1}^R m_{c,r} \right). \quad (3.4)$$

Finally, the image roughness (IR) of the background was calculated as in [18].

Similar considerations were used for the determination of the cold contrast for the real studies investigated. For the Jaszczak phantom, we employed ROIs similar to the ones of the simulations. For the clinical myocardial study, we performed an ROI analysis as follows: we selected a circular region in the centre of the area of the left ventricle of the patient. This area corresponds to the uptake of the cold region. Then, we manually drew an ROI in the myocardial area over the annulus, which corresponds to the warm background area of the heart. We drew similar ROIs for three consecutive slices and averaged the cold contrast measurements, as in equation (3.2).

4. Results

4.1. Simulations

The reconstruction time per slice, for a 45-projections sinogram was 2.3 s for aSRT, 3.7 s for OSEM20, 5.2 s for OSEM30, and 13.7 s for attenuation-corrected FBP (using an Intel[®] Xeon[®] CPU E3-1241 processor, 16 GB RAM). The longer time in FBP reconstructions is due to the fact that the attenuation correction was performed in Matlab. Therefore, in this case, aSRT was faster than both OSEM and FBP.

The simulated IQ phantom is presented in figure 2a, and the corresponding attenuation map is presented in figure 2b. The ROIs employed in order to determine the image metrics are shown in figure 2c. Reconstructed images using aSRT, FBP, and OSEM with 10, 20, 30 and 50 iterations for the IQ phantom, for all numbers of views (45, 90 and 180) are presented in figure 3 for noise level 2 (NL2) and in figure 4 for noise level 3 (NL3). The images presented in these figures are characteristic reconstructions of one (out of twenty) Poisson-noise realizations at each noise level. In all the reconstructed images presented, the all-black colour represents zero values, whereas the value of the all-white colour represents the maximum value of the IQ phantom. Therefore, the scale used in figures 3 and 4 is the same for all sub-images involved.

The contrast and bias for the hot 25.4 mm (S_4) and the cold 38 mm (S_6) spheres as a function of image roughness for 90 and 180 views are presented in figures 5 and 6 respectively, for the various reconstruction techniques used. In each plot, the leftmost datum point in each curve corresponds to NL1, the midpoint to NL2, and the rightmost to NL3.

4.2. Real data

4.2.1. Real Jaszczak phantom

aSRT and FBP reconstructions of the real Jaszczak phantom, as well as the corresponding attenuation map (CT) and ROIs, are presented in figure 7. We note that OSEM reconstructions

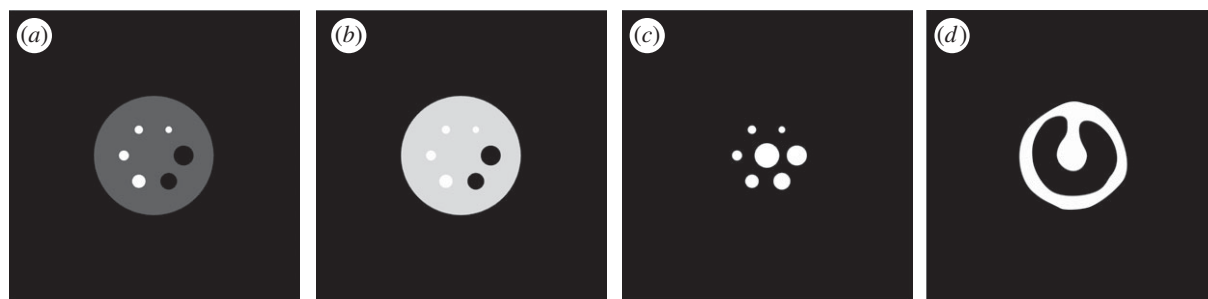


Figure 2. (a) IQ phantom, indicating four hot (white) and two cold regions (black) inside warm background (dark grey). (b) Attenuation map for the IQ phantom simulations, indicating four hot (white) and two cold regions (black) inside warm a background (light grey), corresponding to linear attenuation coefficient values μ (cm^{-1}) of 0.176, 0 and 0.154, respectively. (c,d) Circular ROIs employed for the calculation of image metrics.

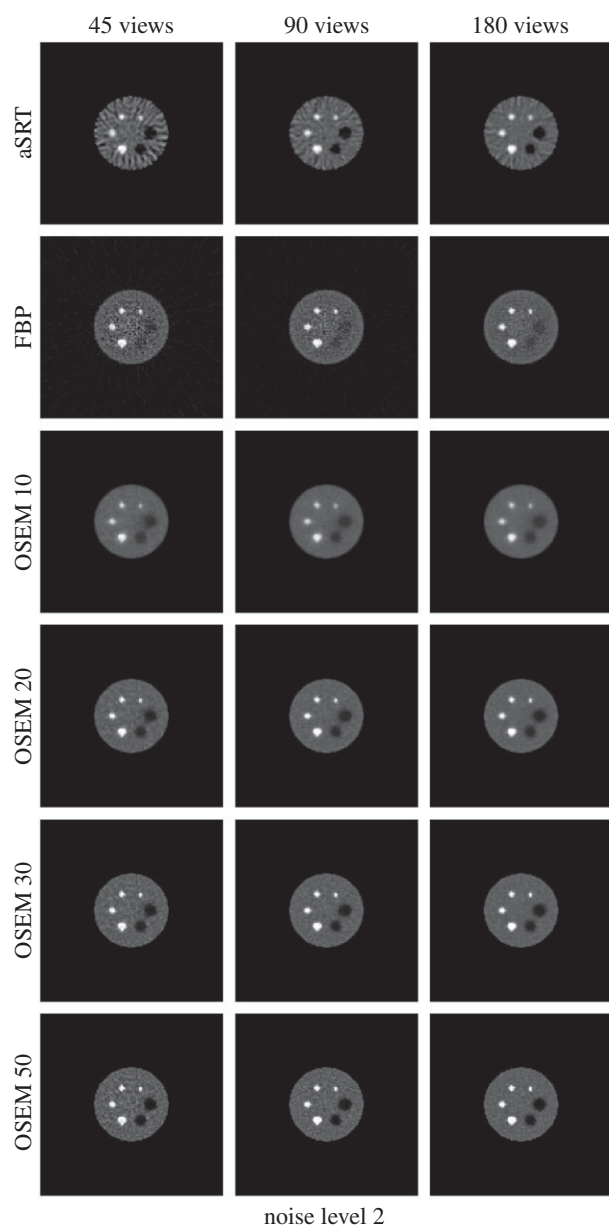


Figure 3. IQ phantom reconstructions at noise level 2 (NL2, 50% of counts) with various reconstruction methods (aSRT, FBP and OSEM with 10, 20, 30 and 50 iterations) at 45, 90 and 180 views.

for the Jaszczak phantom were unavailable. This specific phantom study is a typical cold study, hence only cold contrast is measured.

Cold contrast (C_c) and bias measurements for the six cold spheres of the real Jaszczak phantom for the reconstruction techniques used are presented in figure 8*a,b*, respectively.

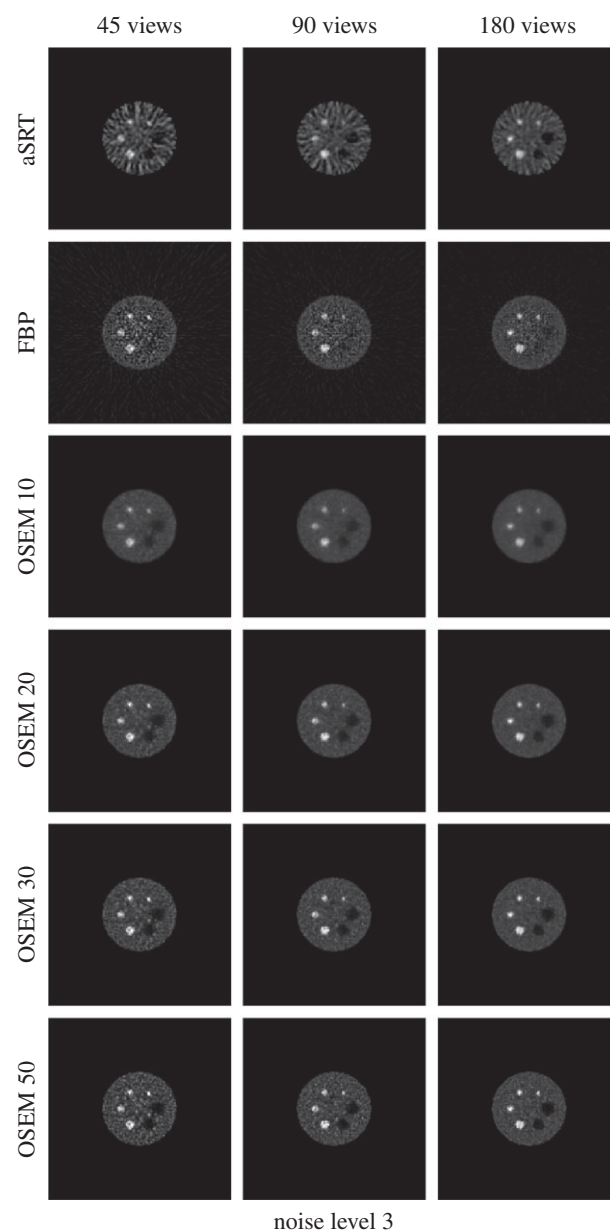


Figure 4. IQ phantom reconstructions at noise level 3 (NL3, 10% of counts) with various reconstruction methods (aSRT, FBP and OSEM with 10, 20, 30 and 50 iterations) at 45, 90 and 180 views.

4.2.2. Clinical data

aSRT, FBP, OSEM (10 iterations) reconstructions, as well as the corresponding attenuation map (CT) and ROIs of the real clinical cardiac data, acquired from a GE Millennium VG Hawkeye™ SPECT/CT system, are presented in

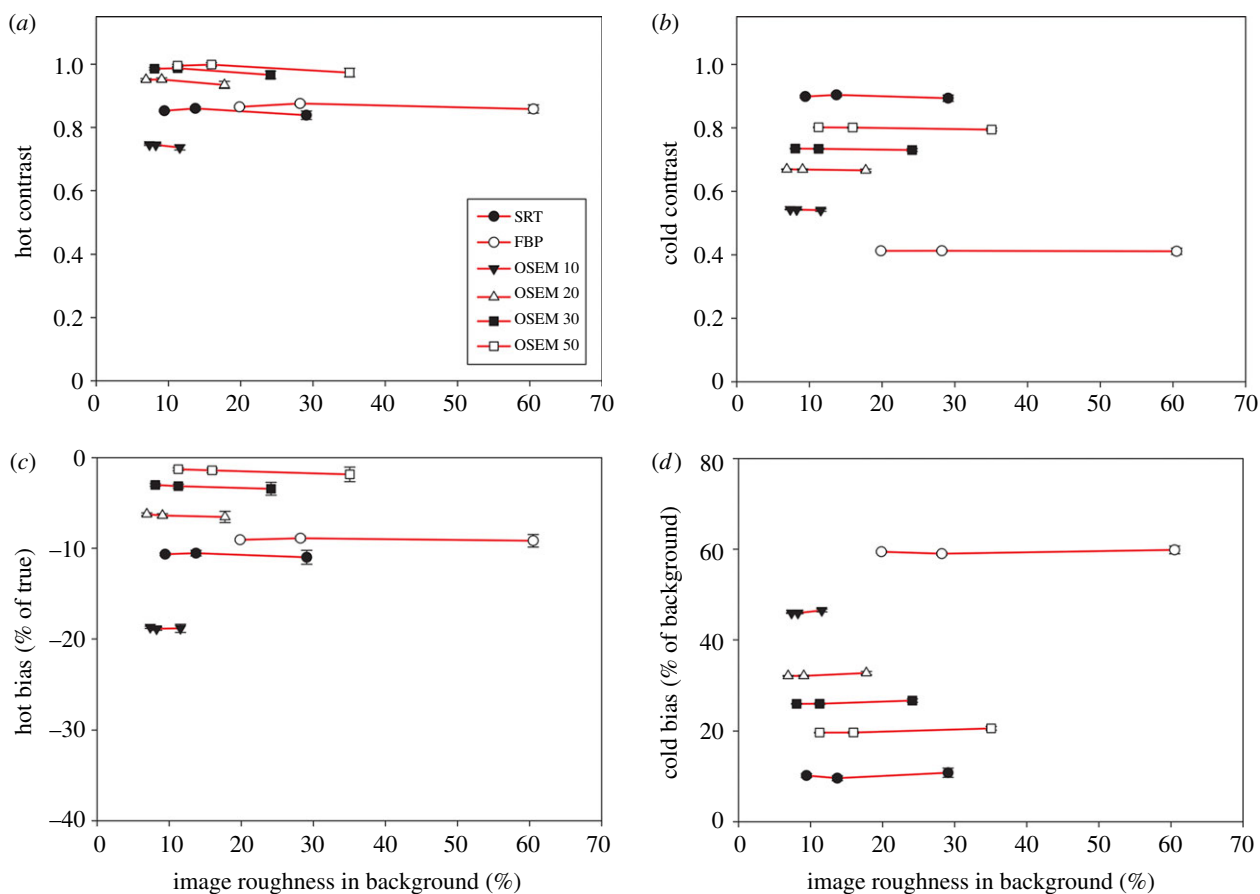


Figure 5. Contrast (C) and bias (b) measurements versus image roughness (IR) at 90 views for the hot sphere S_4 and for the cold sphere S_6 . The leftmost datum point in each curve corresponds to NL1, the midpoint to NL2 and the rightmost to NL3. (a) Hot sphere 4 (S_4) hot contrast, (b) cold sphere 6 (S_6) cold contrast, (c) hot sphere 4 (S_4) hot bias and (d) cold sphere 6 (S_6) cold bias. (Online version in colour.)

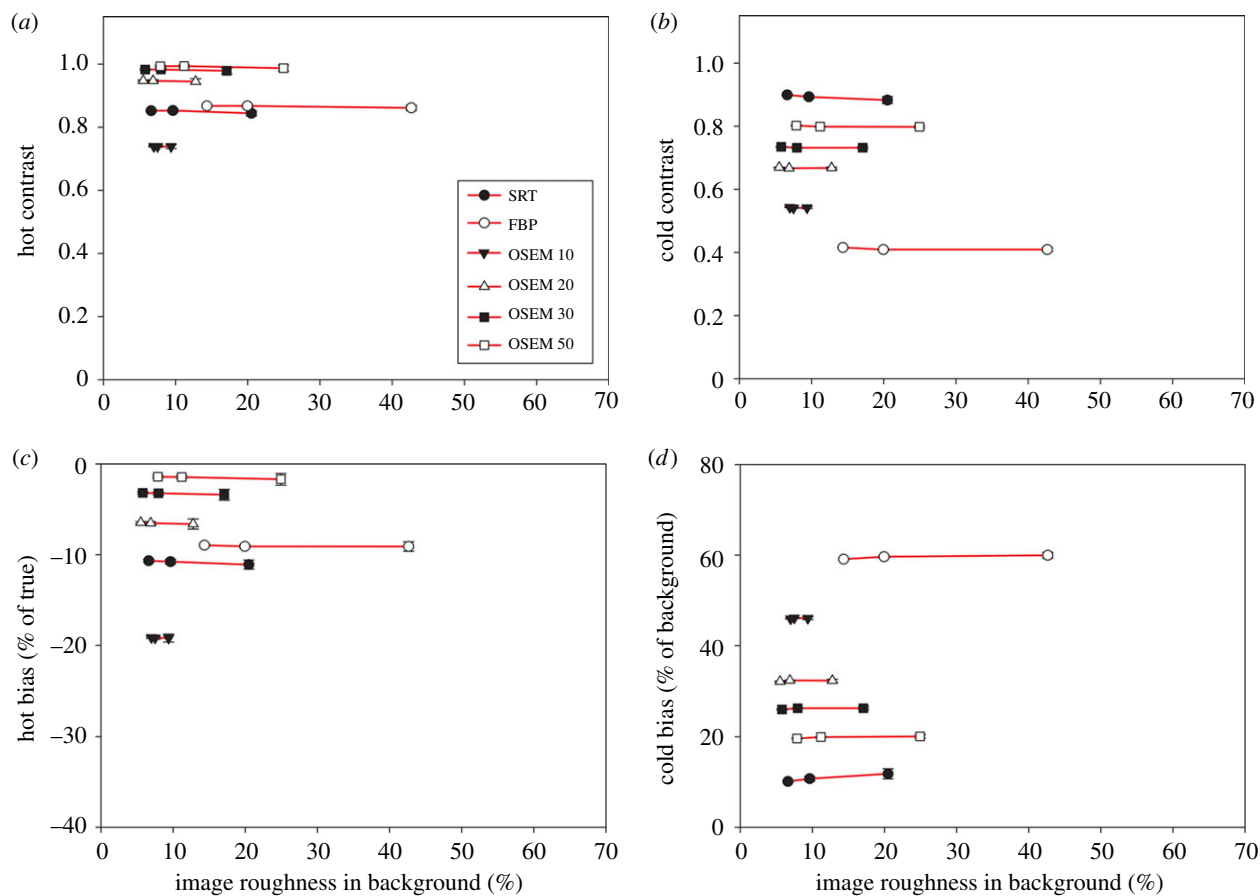


Figure 6. Contrast (C) and bias (b) measurements versus image roughness (IR) at 180 views for the hot sphere S_4 and for the cold sphere S_6 . The leftmost datum point in each curve corresponds to NL1, the midpoint to NL2 and the rightmost to NL3. (a) Hot sphere 4 (S_4) hot contrast, (b) cold sphere 6 (S_6) cold contrast, (c) hot sphere 4 (S_4) hot bias and (d) cold sphere 6 (S_6) cold bias. (Online version in colour.)

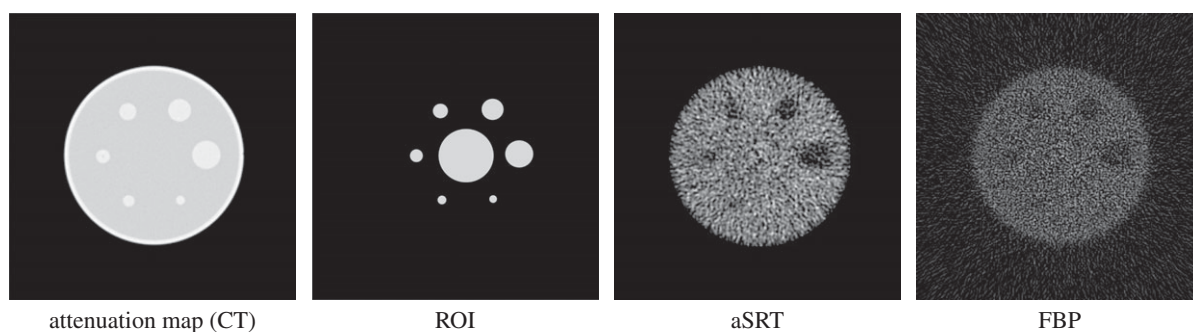


Figure 7. Attenuation map, ROI and reconstructions of a real Jaszczak phantom, cold spheres' region.

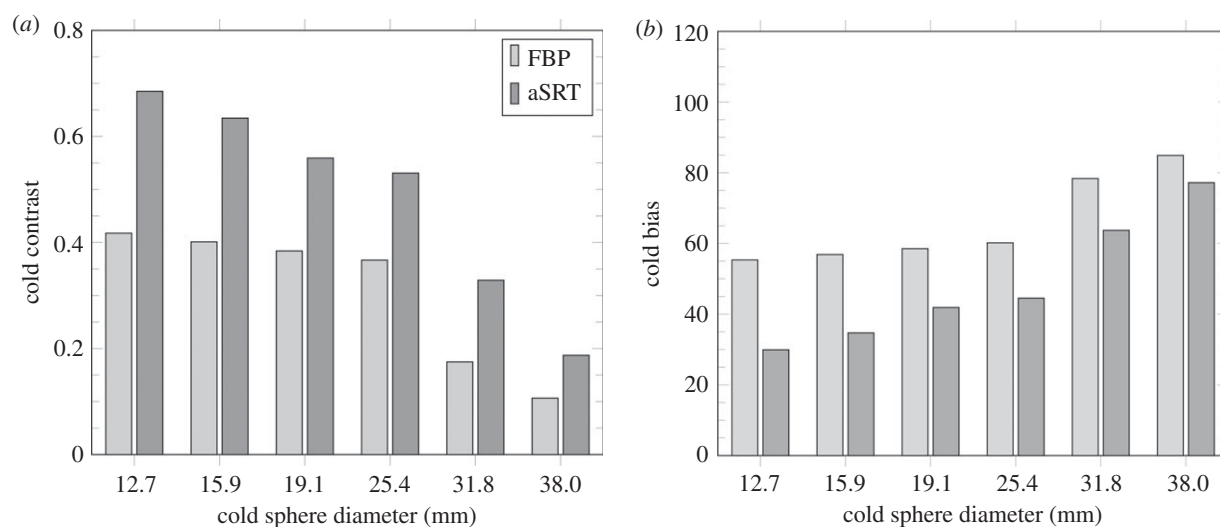


Figure 8. Cold contrast (a) and cold bias (b) measurements for the six cold spheres of the real Jaszczak phantom.

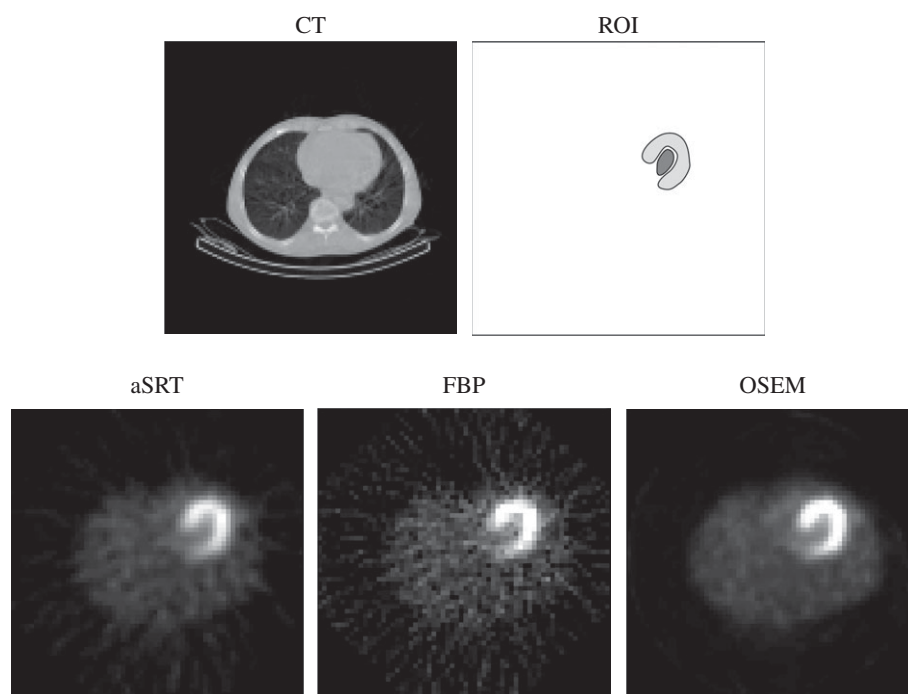


Figure 9. Attenuation map, ROI and reconstructions of real clinical cardiac data, acquired from a GE Millennium VG Hawkeye™ SPECT/CT system.

figure 9. Furthermore, in order to quantify the effect of each reconstruction technique presented, we have performed cold contrast analysis and calculations in this myocardial study. The corresponding results are indicated in figure 10.

5. Discussion

For the simulation studies, in all images presented, it is evident that all hot circular regions can be clearly identified at all noise

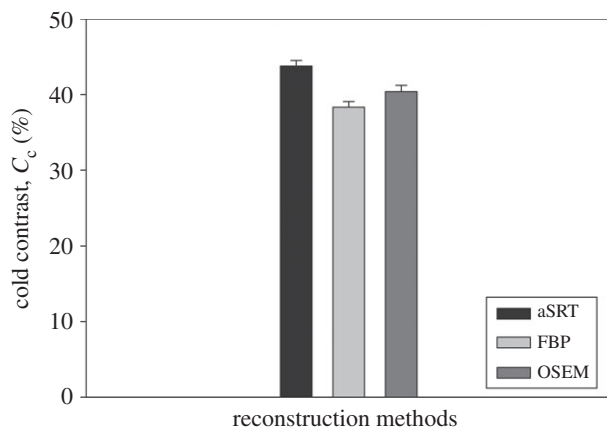


Figure 10. Cold contrast measurements for the real clinical myocardial study.

levels by all reconstruction algorithms. However, the cold regions reconstructed with FBP are not shown clearly, especially in the case of NL3 at 45 views. Some streak artefacts at the edge of the phantom appear in the aSRT reconstructions, especially at a low number of projection angles (views). These streak artefacts are due to incomplete data measurement (angular undersampling [25]) and are closely related to the backprojection operator (integral over theta). Similar streak artefacts are present at a low number of projections in all analytic reconstructions that utilize a backprojection operator, such as FBP and Natterer's inversion formula. It is important to note that the cases of NL3 are unrealistic, especially in 45 views, corresponding to an extremely low number of 3.333 counts per projection.

Overall, FBP reconstructions exhibited higher image roughness at all noise levels and all numbers of projections. Furthermore, the image roughness of aSRT reconstructions is similar to the image roughness of OSEM50 reconstructions, for all noise levels. As expected, the noise level in the variations of OSEM reconstructed images increases as the number of iterations increases. The contrast increases as the number of OSEM iterations increases, whereas the bias decreases, in both hot and cold regions. For all reconstruction techniques used and for all noise levels, the image roughness, represented in the x -axis in figures 5 and 6, increases as the number of views decreases. This is expected, due to lower angular sampling.

For the cold regions of the IQ phantom, aSRT provided images with higher contrast and lower bias than FBP and OSEM for all iteration updates investigated. Both the cold region contrast and the cold bias exhibited, as expected, small variations as a function of the initial noise level of the sinograms. For the 38 mm cold circular region (S_6), the aSRT-reconstructed images exhibited a cold contrast (C_c) of 0.89, which was higher than the contrast of *all* other reconstruction techniques. For the FBP-reconstructed images, the contrast was substantially low (0.41) for S_6 . The OSEM contrast varied from 0.54 for OSEM10 to 0.79 for OSEM50. Similarly, the cold bias % of background (b_c) value for aSRT was the lowest of all other techniques studied (10.80%), whereas for FBP was the highest (59.85%). The OSEM cold bias % of background values varied from 46.49% for OSEM10 to 20.59% for OSEM50. Hence, for the cold regions, aSRT provides better quality images in terms of both contrast and bias.

For the hot regions of the IQ phantom, aSRT provided images with contrast and bias similar to FBP. However, those values for FBP are achieved at the expense of

substantially increasing the image roughness. Both the hot contrast (C_h) and the hot %bias (b_h) for aSRT was, in all cases, between OSEM10 and OSEM20. All hot lesions investigated demonstrated negative hot bias, i.e. $b_h < 0$. The contrast, as well as the bias, demonstrated negligible variations as functions of the sinogram noise level. For the 25.48 mm hot circular lesion (S_4), the hot contrast value was 0.84 for aSRT, 0.86 for FBP, and from 0.74 for OSEM10 to 0.97 for OSEM50. In addition, the hot %bias value was -10.98% for aSRT, -9.17% for FBP, and from -18.83% for OSEM10 to -1.84% for OSEM50. FBP exhibited similar contrast to aSRT, although at the expense of higher levels of image roughness. It is important to note that the ROI placement for the background affects the image roughness of aSRT. Selecting a background ROI which includes the central region of the phantom, as well as areas at the edge of the object (streaking artefacts) results in an increase in image roughness for aSRT; see figure 2*d*. More specifically, the new image roughness values for NL1 to NL3 were: (i) for 90 views, 13.53%, 18.74% and 40.54%, respectively, and (ii) for 180 views, 9.43%, 13.31% and 28.87%, respectively. These values for aSRT image roughness are still lower than the corresponding ones of FBP. In the cases of FBP and OSEM, the corresponding values of IR remained unchanged, as expected. It should be noted that contrast and bias measurements are not affected by the choice of background ROI.

For the real Jaszczak phantom study, the FBP-reconstructed image exhibited substantially higher image roughness (0.96) than the one reconstructed with aSRT (0.51). It is evident that for the cold Jaszczak phantom study, the contrast and bias measured in aSRT reconstructions are superior to the ones in FBP reconstructions in all cold spheres investigated; see figure 8*a,b*, respectively.

For the clinical myocardial ^{201}Tl stress test perfusion SPECT/CT study, aSRT exhibited a cold contrast (C_c) of about 44%, FBP of about 38% and OSEM of about 40% (see figure 10). Therefore, aSRT exhibited cold contrast improvement of about 14% over FBP and 8% improvement over OSEM. Hence, it is evident that in cold cardiac regions, aSRT produces images with higher cold contrast than both FBP and OSEM. It is important to note that, among the relevant literature of analytic inversion of the attenuated Radon transform, aSRT was the only algorithm to be tested with reconstructions of clinical SPECT/CT data. The improvement of our method over FBP and OSEM is an indication that aSRT may be valuable in the imaging of graded structures *in vivo* (e.g. nucleus and annulus of spines, mitral valves etc.). Furthermore, we note that for the clinical studies no artefacts were present, indicating that some of the simulated cases studied suffered from 'unrealistic' high noise and small number of projections (cases chosen to investigate the limitations of our algorithm).

Overall, the improvement in contrast and bias of the cold regions of aSRT over OSEM can be explained by recalling that OSEM exhibits slow convergence in regions of low counts due to the positivity constraint imposed by the algorithm.

6. Conclusion

aSRT is a novel, fast analytic algorithm capable of reconstructing attenuation-corrected SPECT/CT images. In the present work, we have compared aSRT with FBP and OSEM using simulated

and real phantoms, as well as real clinical data. We have presented an improved version of the analytic formula of the IART and have implemented aSRT in Matlab. We have evaluated the aSRT reconstructions in comparison with FBP and OSEM reconstructions using contrast, bias and image roughness.

Our tests suggest that aSRT can efficiently produce accurate attenuation-corrected reconstructions for simulated phantoms as well as real data. In particular, it appears that aSRT has a considerable advantage in cold regions in comparison with both FBP and our implementation of OSEM. More specifically, the aSRT results of the clinical myocardial study are encouraging, indicating that aSRT could provide useful reconstructions in a real clinical setting. Further investigation is needed to better quantify with the help of physicians, the improvement of aSRT in myocardial imaging. Clinical studies involving myocardial ischaemia are in progress, where the advantage of aSRT for cold regions should be demonstrated via receiver operating characteristics curves. Overall, aSRT may provide an improved alternative to FBP for SPECT reconstruction.

Data accessibility. We intend to implement our algorithm in STIR and make it publicly available in the future. All reconstructed images, data and code involved have been uploaded as part of the electronic supplementary material.

Authors' contributions. N.E.P., A.S.F. and G.A.K. conceived, designed and supervised the study. N.E.P., K.K. and G.A.K. performed experiments and analysis. N.E.P. wrote the initial draft of the manuscript. All authors critically revised and improved the manuscript in various

ways. All authors reviewed the manuscript and gave final approval for publication.

Competing interests. We declare we have no competing interests.

Funding. A.S.F. acknowledges support from EPSRC via a senior fellowship. G.A.K. was supported by the Onassis Foundation (grant no. R ZL 001-1/2015-2016). This work was partially supported by the research programme 'Inverse Problems and Medical Imaging' (200/855) of the Research Committee of the Academy of Athens.

Acknowledgements. The authors would like to thank Theodore Skouras (Medical Physics Department of the University Hospital of Patras) for providing the real SPECT/CT data, as well as Dr Anastasios Gaitanis (Biomedical Research Foundation of the Academy of Athens) for his assistance in real data acquisition. In addition, the authors would like to thank Miklos Kovacs, Gabor Nemeth and Andras Wirth (Mediso Medical Imaging Systems, Budapest) for providing the real phantom data. Furthermore, the authors are grateful to Dr Vangelis Marinakis (Technological Educational Institute of Western Greece) whose earlier code provided the starting point for the numerical part of the present studies.

Appendix A

In order to simplify equation (2.9), we first combine equations (2.10) and (2.11) and rewrite L_μ in the form

$$(L_\mu \hat{f}_\mu)(\rho, \theta) = \frac{1}{2i} e^{-\hat{\mu}/2} [e^{-iF} \mathcal{H}\{e^{\hat{\mu}/2+iF} \hat{f}_\mu\} + e^{iF} \mathcal{H}\{e^{\hat{\mu}/2-iF} \hat{f}_\mu\}]. \quad (\text{A } 1)$$

Using $e^{\pm iF} = \cos F \pm i \sin F$, equation (A 1) simplifies as follows:

$$\begin{aligned} (L_\mu \hat{f}_\mu)(\rho, \theta) &= \frac{1}{2i} e^{-\hat{\mu}/2} [(\cos F - i \sin F) \mathcal{H}\{e^{\hat{\mu}/2+iF} \hat{f}_\mu\} + (\cos F + i \sin F) \mathcal{H}\{e^{\hat{\mu}/2-iF} \hat{f}_\mu\}] \\ &= \frac{1}{2i} e^{-\hat{\mu}/2} [\cos F (\mathcal{H}\{e^{\hat{\mu}/2+iF} \hat{f}_\mu\} + \mathcal{H}\{e^{\hat{\mu}/2-iF} \hat{f}_\mu\}) - i \sin F (\mathcal{H}\{e^{\hat{\mu}/2+iF} \hat{f}_\mu\} - \mathcal{H}\{e^{\hat{\mu}/2-iF} \hat{f}_\mu\})] \\ &= \frac{1}{2\pi i} e^{-\hat{\mu}/2} \left[\cos F \oint_{-\infty}^{\infty} \frac{e^{\hat{\mu}/2+iF} + e^{\hat{\mu}/2-iF}}{r - \rho} \hat{f}_\mu \, dr - i \sin F \oint_{-\infty}^{\infty} \frac{e^{\hat{\mu}/2+iF} - e^{\hat{\mu}/2-iF}}{r - \rho} \hat{f}_\mu \, dr \right] \\ &= \frac{1}{2\pi i} e^{-\hat{\mu}/2} \left[\cos F \oint_{-\infty}^{\infty} \frac{e^{\hat{\mu}/2} (e^{iF} + e^{-iF})}{r - \rho} \hat{f}_\mu \, dr - i \sin F \oint_{-\infty}^{\infty} \frac{e^{\hat{\mu}/2} (e^{iF} - e^{-iF})}{r - \rho} \hat{f}_\mu \, dr \right] \\ &= \frac{1}{2\pi i} e^{-\hat{\mu}/2} \left[\cos F \oint_{-\infty}^{\infty} \frac{e^{\hat{\mu}/2} (2 \cos F)}{r - \rho} \hat{f}_\mu \, dr - i \sin F \oint_{-\infty}^{\infty} \frac{e^{\hat{\mu}/2} (2i \sin F)}{r - \rho} \hat{f}_\mu \, dr \right] \\ &= \frac{2}{i} e^{-\hat{\mu}/2} \left[\cos F \left(\frac{1}{2\pi} \oint_{-\infty}^{\infty} \frac{e^{\hat{\mu}/2} \cos F}{r - \rho} \hat{f}_\mu \, dr \right) + \sin F \left(\frac{1}{2\pi} \oint_{-\infty}^{\infty} \frac{e^{\hat{\mu}/2} \sin F}{r - \rho} \hat{f}_\mu \, dr \right) \right] \\ &= -2i e^{-\hat{\mu}/2} [\cos(F) G^C + \sin(F) G^S], \end{aligned}$$

with G , $G^C(\rho, \theta)$ and $G^S(\rho, \theta)$ defined in equations (2.7), (2.8a) and (2.8b), respectively. Hence, equation (2.9) becomes equation (2.12).

Appendix B

We assume that a function $f: [-1, 1] \times [0, 2\pi] \rightarrow \mathbb{R}$, with arguments indicated by (ρ, θ) , is given for every θ at the n points $\{\rho_i\}_1^n$. We denote the value of f at ρ_i by f_i , i.e.

$$f_i(\theta) = f(\rho_i, \theta), \quad \rho_i \in [-1, 1], \quad 0 \leq \theta < 2\pi, \quad (\text{B } 1)$$

$$i = 1, \dots, n.$$

Furthermore, we assume that both $f(\rho, \theta)$ and its derivative

with respect to ρ vanish at the endpoints $\rho_1 = -1$ and $\rho_n = 1$:

$$f(-1, \theta) = f(1, \theta) = 0, \quad 0 \leq \theta < 2\pi \quad (\text{B } 2a)$$

and

$$\frac{\partial f}{\partial \rho}(-1, \theta) = \frac{\partial f}{\partial \rho}(1, \theta) = 0, \quad 0 \leq \theta < 2\pi. \quad (\text{B } 2b)$$

In the interval $\rho_i \leq \rho \leq \rho_{i+1}$, for all $i = 1, \dots, n-1$, we approximate $f(\rho, \theta)$ by cubic splines, $S_i^{(3)}(\rho, \theta)$, in the variable ρ :

$$f(\rho, \theta) \sim S_i^{(3)}(\rho, \theta) \quad \rho_i \leq \rho \leq \rho_{i+1}, \quad 0 \leq \theta < 2\pi.$$

This cubic spline interpolates the function $f(\rho, \theta)$ at the knots

$\{\rho_i\}_{i=1}^n$ in the sense that

$$S_i^{(3)}(\rho_i, \theta) = f_i(\theta), \quad i = 1, \dots, n-1. \quad (\text{B3})$$

More specifically,

$$S_i^{(3)}(\rho, \theta) = \sum_{j=0}^3 c_i^{(j)} \rho^j \quad \rho_i \leq \rho \leq \rho_{i+1}, \quad 0 \leq \theta < 2\pi, \quad (\text{B4})$$

where the constants $\{c_i^{(j)}\}_{i=1}^n$ for $j = 0, \dots, 3$ are given by the following expressions [21]:

$$c_i^{(0)} = \frac{\rho_{i+1}f_i - \rho_i f_{i+1}}{\Delta_i} + \frac{f_i''}{6} \left(-\rho_{i+1}\Delta_i + \frac{\rho_{i+1}^3}{\Delta_i} \right) + \frac{f_{i+1}''}{6} \left(\rho_i\Delta_i - \frac{\rho_i^3}{\Delta_i} \right), \quad (\text{B5a})$$

$$c_i^{(1)} = \frac{f_{i+1} - f_i}{\Delta_i} - \frac{f_i''}{6} \left(-\Delta_i + \frac{3\rho_{i+1}^2}{\Delta_i} \right) + \frac{f_{i+1}''}{6} \left(-\Delta_i + \frac{3\rho_i^2}{\Delta_i} \right), \quad (\text{B5b})$$

$$c_i^{(2)} = \frac{1}{2\Delta_i} (\rho_{i+1}f_i'' - \rho_i f_{i+1}''), \quad (\text{B5c})$$

$$c_i^{(3)} = \frac{f_{i+1}'' - f_i''}{6\Delta_i} \quad (\text{B5d})$$

and $\Delta_i = \rho_{i+1} - \rho_i$ (B6)

with f_i'' denoting the second derivative of $f(\rho, \theta)$ with respect to ρ evaluated at ρ_i , i.e.

$$f_i'' = \left. \frac{\partial^2 f(\rho, \theta)}{\partial \rho^2} \right|_{\rho=\rho_i}, \quad i = 1, \dots, n. \quad (\text{B7})$$

Equation (B 4) implies

$$\oint_{\rho_i}^{\rho_{i+1}} \frac{f(r, \theta)}{r - \rho} dr \sim \sum_{j=0}^3 c_i^{(j)} I_i^{(j)}(\rho), \quad (\text{B8})$$

where

$$I_i^{(j)}(\rho) = \oint_{\rho_i}^{\rho_{i+1}} \frac{r^j}{r - \rho} dr, \quad j = 0, \dots, 3. \quad (\text{B9})$$

Straightforward calculations yield the following identities for the integrals defined in (B 9):

$$I_i^{(0)}(\rho) = \ln \left| \frac{\rho_{i+1} - \rho}{\rho_i - \rho} \right|, \quad (\text{B10a})$$

$$I_i^{(1)}(\rho) = \Delta_i + \rho I_i^{(0)}(\rho), \quad (\text{B10b})$$

$$I_i^{(2)}(\rho) = \frac{1}{2} (\rho_{i+1}^2 - \rho_i^2) + \Delta_i \rho + \rho^2 I_i^{(0)}(\rho) \quad (\text{B10c})$$

and $I_i^{(3)}(\rho) = \frac{1}{3} (\rho_{i+1}^3 - \rho_i^3) + \frac{1}{2} (\rho_{i+1}^2 - \rho_i^2) \rho + \Delta_i \rho^2 + I_i^{(0)}(\rho) \rho^3$. (B10d)

Substituting equations (B 9) and (B 10) in equation (B 8) we find

$$\oint_{\rho_i}^{\rho_{i+1}} \frac{f(r, \theta)}{r - \rho} dr \sim \alpha_i(\theta) + \beta_i(\theta)\rho + \gamma_i(\theta)\rho^2 + \left(\sum_{j=0}^3 c_i^{(j)} \rho^j \right) I_i^{(0)}(\rho), \quad (\text{B11})$$

where

$$\alpha_i(\theta) = c_i^{(1)}(\theta)\Delta_i + \frac{1}{2}c_i^{(2)}(\theta)(\rho_{i+1}^2 - \rho_i^2) + \frac{1}{3}c_i^{(3)}(\theta)(\rho_{i+1}^3 - \rho_i^3), \quad (\text{B12})$$

$$\beta_i(\theta) = (c_i^{(2)}(\theta)\Delta_i + \frac{1}{2}c_i^{(3)}(\theta)(\rho_{i+1}^2 - \rho_i^2)) \quad (\text{B13})$$

and $\gamma_i(\theta) = c_i^{(3)}(\theta)\Delta_i$. (B14)

Taking into account equations (B 5), the above expressions simplify as follows:

$$\alpha_i(\theta) = (f_{i+1} - f_i) - \frac{1}{36} [17\rho_{i+1}^2 - 19\rho_{i+1}\rho_i + 8\rho_i^2] f_i'' - \frac{1}{36} [4\rho_{i+1}^2 - 5\rho_{i+1}\rho_i - 5\rho_i^2] f_{i+1}'', \quad (\text{B15})$$

$$\beta_i(\theta) = \frac{1}{12} [(5\rho_{i+1} - \rho_i) f_i'' - (5\rho_i - \rho_{i+1}) f_{i+1}''] \quad (\text{B16})$$

and $\gamma_i(\theta) = \frac{f_{i+1}'' - f_i''}{6}$. (B17)

Hence, using the identity

$$\oint_{-1}^1 \frac{f(r, \theta)}{r - \rho} dr = \sum_{i=1}^{n-1} \oint_{\rho_i}^{\rho_{i+1}} \frac{f(r, \theta)}{r - \rho} dr, \quad (\text{B18})$$

equation (B 11) implies

$$\begin{aligned} \oint_{-1}^1 \frac{f(r, \theta)}{r - \rho} dr &\sim A(\theta) + B(\theta)\rho + \frac{1}{6} (f_n'' - f_1'') \rho^2 \\ &+ \sum_{i=1}^{n-2} [S_i^{(3)}(\rho, \theta) - S_{i+1}^{(3)}(\rho, \theta)] \ln |\rho_{i+1} - \rho| \\ &+ S_{n-1}^{(3)}(\rho, \theta) \ln |\rho_n - \rho| - S_1^{(3)}(\rho, \theta) \ln |\rho_1 - \rho|, \end{aligned} \quad (\text{B19})$$

where

$$A(\theta) = \sum_{i=1}^{n-1} \alpha_i(\theta) \quad \text{and} \quad B(\theta) = \sum_{i=1}^{n-1} \beta_i(\theta). \quad (\text{B20})$$

The right-hand-side of equation (B 19) involves the functions $\{f_i\}_1^n$, which are known, and the functions $\{f_i''\}_1^n$, which are unknown. If we denote the derivative of the cubic spline, $S_i^{(3)}$, by $S_i^{(2)}$, where the superscript denotes that $S_i^{(2)}$ is quadratic, then we find

$$S_i^{(2)}(\rho, \theta) = \frac{\partial S_i^{(3)}(\rho, \theta)}{\partial \rho} = c_i^{(1)}(\theta) + 2c_i^{(2)}(\theta)\rho + 3c_i^{(3)}(\theta)\rho^2. \quad (\text{B21})$$

In order to compute $\{f_i''\}_1^n$ we follow the procedure of [17], namely we solve the system of the following n equations (continuity of the first derivative of the cubic spline):

$$S_i^{(2)}(\rho_{i+1}, \theta) = S_{i+1}^{(2)}(\rho_{i+1}, \theta), \quad i = 1, \dots, n-2, \quad 0 \leq \theta < 2\pi \quad (\text{B22a})$$

and

$$S_1^{(2)}(\rho_1, \theta) = S_{n-1}^{(2)}(\rho_n, \theta) = 0. \quad (\text{B22b})$$

The continuity of the spline, namely $S_i^{(3)}(\rho_{i+1}, \theta) = S_{i+1}^{(3)}(\rho_{i+1}, \theta)$ for $i = 1, \dots, n-2$, and $S_1^{(3)}(\rho_1, \theta) = S_{n-1}^{(3)}(\rho_n, \theta) = 0$ (see equations (B 2a)), implies that the points $\{\rho_i\}_1^n$ are removable logarithmic singularities.

Using equation (B 19) with $f(\rho, \theta) = \hat{\mu}(\rho, \theta)$ we can compute $F(\rho, \theta)$.

1. Phelps ME. 2006 *PET: physics, instrumentation, and scanners*. New York, NY: Springer.
2. Iniewski K. 2009 *Medical imaging: principles, detectors, and electronics*. New York, NY: Wiley-Interscience.
3. Barrett HH, Myers KJ. 2004 *Foundations of image science*. New York, NY: Wiley.
4. Cuocolo A. 2011 Attenuation correction for myocardial perfusion SPECT imaging: still a controversial issue. *Eur. J. Nucl. Med. Mol. Imaging* **38**, 1887–1889. (doi:10.1007/s00259-011-1898-6)
5. Germano G, Slomka PJ, Bermans DS. 2007 Attenuation correction in cardiac SPECT: the boy who cried wolf? *J. Nucl. Cardiol.* **14**, 25–35. (doi:10.1016/j.nuclcard.2006.12.317)
6. Wacker F. 1999 Attenuation correction, or the emperor's new clothes? [editorial]. *J. Nucl. Med.* **40**, 1310–1312.
7. Hendel RC. 2005 Attenuation correction: eternal dilemma or real improvement? *Q. J. Nucl. Med. Mol. Imaging* **49**, 30–42.
8. Mariani G, Bruselli L, Kuwert T, Kim EE, Flotats A, Israel O, Dondi M, Watanabe N. 2010 A review on the clinical uses of SPECT/CT. *Eur. J. Nucl. Med. Mol. Imaging* **37**, 1959–1985. (doi:10.1007/s00259-010-1390-8)
9. Fokas A, Iserles A, Marinakis V. 2006 Reconstruction algorithm for single photon emission computed tomography and its numerical implementation. *J. R. Soc. Interface* **3**, 45–54. (doi:10.1098/rsif.2005.0061)
10. Novikov R. 2002 An inversion formula for the attenuated X-ray transformation. *Ark. Mat.* **40**, 145–167. (doi:10.1007/BF02384507)
11. Natterer F. 2001 Inversion of the attenuated Radon transform. *Inverse Probl.* **17**, 113–119. (doi:10.1088/0266-5611/17/1/309)
12. Kunyansky LA. 2001 A new SPECT reconstruction algorithm based on the Novikov explicit inversion formula. *Inverse Probl.* **17**, 293–306. (doi:10.1088/0266-5611/17/2/309)
13. Tretiak O, Metz C. 1980 The exponential Radon transform. *SIAM J. Appl. Math.* **39**, 341–354. (doi:10.1137/0139029)
14. Metz CE, Pan X. 1995 A unified analysis of exact methods of inverting the 2-D exponential Radon transform, with implications for noise control in SPECT. *IEEE Trans. Med. Imag.* **14**, 643–658. (doi:10.1109/42.476106)
15. Bal G, Moireau P. 2004 Fast numerical inversion of the attenuated Radon transform with full and partial measurements. *Inverse Probl.* **20**, 1137–1164. (doi:10.1088/0266-5611/20/4/009)
16. Ammari H, Bretin E, Jugnon V, Wahab A. 2012 Photoacoustic imaging for attenuating acoustic media. In *Mathematical modeling in biomedical imaging II: optical, ultrasound, and opto-acoustic tomographies* (ed. H Ammari), ch. 3, pp. 57–84. Berlin, Germany: Springer.
17. Kastis GA, Kyriakopoulou D, Gaitanis A, Fernández Y, Hutton BF, Fokas AS. 2014 Evaluation of the spline reconstruction technique for PET. *Med. Phys.* **41**, 042501. (doi:10.1118/1.4867862)
18. Kastis GA, Gaitanis A, Samartzis AP, Fokas AS. 2015 The SRT reconstruction algorithm for semiquantification in PET imaging. *Med. Phys.* **42**, 5970–5982. (doi:10.1118/1.4931409)
19. Fokas A, Novikov R. 1991 Discrete analogues of $\bar{\partial}$ -equation and of Radon transform. *C. R. Acad. Sci. Série 1, Math.* **313**, 75–80.
20. Unser M, Fageot J, Ward JP. 2017 Splines are universal solutions of linear inverse problems with generalized TV regularization. *SIAM Rev.* **59**, 769–793. (doi:10.1137/16M1061199)
21. Press WH, Teukolsky SA, Vetterling WT, Flannery BP. 2007 *Numerical recipes: the art of scientific computing*, 3rd edn. New York, NY: Cambridge University Press.
22. Thielemans K, Tsoumpas C, Mustafovic S, Beisel T, Aguiar P, Dikaios N, Jacobson MW. 2012 STIR: software for tomographic image reconstruction release 2. *Phys. Med. Biol.* **57**, 867–883. (doi:10.1088/0031-9155/57/4/867)
23. Saha K, Hoyt SC, Murray BM. 2016 Application of Chang's attenuation correction technique for single-photon emission computed tomography partial angle acquisition of Jaszczak phantom. *J. Med. Phys.* **41**, 29–33. (doi:10.4103/0971-6203.177278)
24. Zaidi H (ed.). 2006 *Quantitative analysis in nuclear medicine imaging*. Berlin, Germany: Springer.
25. Cherry S, Sorenson J, Phelps M. 2003 *Physics in nuclear medicine*, 3rd edn. Amsterdam, The Netherlands: Elsevier Health Sciences.